Image Restoration for the MRA-Based Pansharpening Method

JIAO JIAO[ID] AND LINGDA WU
Science and Technology on Complex Electronic System Simulation Laboratory, Space Engineering University, Beijing 101416, China

Corresponding author: Jiao Jiao (jiaojiao_nk@163.com)

ABSTRACT By merging high-resolution panchromatic (PAN) images with low-resolution multi-spectral (MS) images, high-resolution MS images with complementary information can be obtained, i.e., pansharpening. Multiresolution analysis (MRA) methods have attracted widespread attention in the pansharpening field. The spatial detail information injected into MS images is extracted from PAN images by MRA tools. Since such methods often suffer from spatial distortion and ringing artifacts, a restoration algorithm based on blind deblurring and iterative back-projection (IBP) is proposed in this paper. First, a blind deblurring method based on the Tikhonov regular constraint model is used to estimate the blurring filter. Second, spatial details extracted from PAN images are modulated into MS images using a high-pass modulation (HPM) framework, and then fusion images are spatially enhanced based on the modulation results and blurring filter. Finally, the IBP technique is used to project the reconstruction error back to iteratively update and optimize the desired high-resolution images. Experiments are performed on data sets acquired by different satellites at full and reduced resolution, and eight state-of-the-art MRA-based pansharpening methods are used for validation. Compared to the enhanced back-projection (EBP) algorithm, the proposed restoration method is better in improving spectral and spatial quality of MRA-based pansharpening. The results indicate the effectiveness and superiority of the proposed method.

INDEX TERMS Blind deblurring, image restoration, iterative back-projection, multiresolution analysis, pansharpening.

I. INTRODUCTION

With the rapid development in image sensor and imaging technology, it is convenient for optical remote sensing satellites to obtain massive images. Thus, the time, space and spectral resolution are greatly improved. The accumulation of massive remote sensing data provides support for accurate interpretation of ground objects, including classification and recognition. Due to physical and technical limitations, optical remote sensing satellites such as QuickBird, IKONOS, GeoEye and WorldView cannot provide remote sensing images with both high spectral and high spatial resolution. Panchromatic (PAN) and multispectral (MS) images are two kinds of typical optical satellite images with different spatial and spectral properties. By combining spatial and spectral information of MS and PAN images while removing the redundancy, MS images with high spatial resolution can

be obtained, which is called pansharpening. Pansharpening belongs to image fusion, also known as superresolution.

In the past two decades, fusion of MS and PAN images has become an important task in the field of data fusion, which has attracted the extensive attention of researchers. The importance of this research is illustrated by the annual data fusion contest organized by the IEEE Geoscience and Remote Sensing Society since 2006. At present, there have been many theories and methods proposed for pansharpening, which can be classified into three categories: the component substitution (CS) method, the multiresolution analysis (MRA) method and the model-based method [2], [3]. Literature [4] systematically reviewed and compared the CS- and MRA-based pansharpening methods. CS-based methods are often referred to as a spectral class, which separates the spectral and spatial components by projecting MS images into a new space and substituting spatial components with the histogram-matched PAN images. This family mainly includes intensity hue saturation (IHS) [5], principal component

The associate editor coordinating the review of this manuscript and approving it for publication was Krishna Kant Singh.

analysis (PCA) [6], Gram–Schmidt (GS) [7], band-dependent spatial detail (BDSD) [8], and Gram–Schmidt adaptive [9]. These methods can be realized easily and can achieve relatively good spatial quality but are more likely to suffer from spectral distortion. MRA-based methods, called spatial class, have better spectral quality than CS-based methods because the spatial detail information injected into MS images is extracted from PAN images by MRA tools. Popular examples in this family are additive wavelet luminance proportional (AWLP) [10], à trous wavelet transform (ATWT) [11], high-pass filtering (HPF) [12], smoothing filter-based intensity modulation (SFIM) [13] and generalized Laplace pyramid (GLP) [14]. MRA methods can achieve better spectral quality but may introduce artifacts into fusion results and suffer from spatial distortion. In fact, CS- and MRA-based methods have strong complementary characteristics in terms of enhancement of spatial details and preservation of spectral properties. Some other fusion methods have also emerged in recent years, such as a Bayesian method based on total variation penalization terms [15], and sparse representation or compressive sensing theory [16], [17]. Although these methods have achieved good fusion effects, the high computational complexity caused by optimization techniques limits their application in practice.

Major challenges related to image sensor and acquisition systems include two aspects: misregistration caused by differences between temporal or spatial coordinate systems of MS and PAN images, and aliasing of MS bands associated with optical properties of MS sensors, which usually results in spectral distortion and jagged edges [18], although the CS family has been proven to be less sensitive than the MRA family to these two problems in general [19], [20]. The pansharpening method, due to its own limitations, may inevitably cause some spectral distortion, artificial texture or excessive injection of spatial details. To a certain degree, loss of useful information and degradation of fusion results may have negative impacts on further applications. To meet the needs of practical applications and obtain more useful information, it is especially important to restore the fusion results. Therefore, image restoration has become an important research work. Several studies have combined fusion methods with restoration in their process flows. The literature [21] incorporated the modulation transfer function (MTF) differences between PAN and MS images into the ARSIS-based scheme and proved that based on this difference, the fusion performance can be improved from the perspective of geometry without degrading the image quality. In the literature [22], estimation of the blurring filter was modeled as an image blind deconvolution problem, and then MS and PAN images were fused based on the estimated filter and high-pass modulation (HPM) injection scheme. In the literature [23], a simple improved scheme was proposed to replace the interpolated MS image with its deblurred version, to improve the pansharpening quality. Approaches mentioned in these studies all belong to restoration methods of preprocessing; there are also some restoration methods used

as a postprocessing step for pansharpening. For example, conditional filtering in the PCA domain was used to enhance the spatial details of fusion results in the literature [18]. Correction of color distortion and noise near the edges was carried out based on the fusion results in the literature [24]. Fusion quality has been improved through the postprocessing step.

This paper focuses on the postprocessing restoration of pansharpening results achieved by MRA-based methods. Considering the disadvantages of the methods in detail injection, it is necessary to focus on enhancing the spatial details of the fusion results while further improving the ability to maintain spectral information. Gaussian-shaped filters are mostly used to approximate the MTF of MS sensors in practical applications. However, the MTF gain at the Nyquist frequency may not always be available for many sensors. Moreover, it may change with the aging of optical and electronic equipment. Thus, using the gain at the Nyquist frequency cannot always make the MTF of sensors achieve the desired accuracy. Therefore, the method proposed in the literature [22] is adopted to simulate the relationship between PAN and MS images to estimate the MTF in this paper. The HPM injection scheme is a well-known modulation model, which is often used to enhance the spatial details of MS images [11], [24]–[26]. In the literature [11], HPM technology was analogized with the contrast of images in local areas, which is generally superior to the HPF method [24]. Therefore, the HPM scheme can be adopted to improve the spatial quality of pansharpening. According to Wald's protocol [27], when a fused image blurs its spatial information and returns to the original MS scale, it should match the original MS image as closely as possible [28]. However, the fusion image still suffers from the loss of spatial precision, which is contrary to spatial consistency. Enhanced back-projection (EBP) technology, proposed in the literature [28], is used to iteratively tune the estimated high-resolution images, and the MTF-matched filters are used to guide the back-projection.

Motivated by the advantages of blind deblurring, the HPM scheme and EBP technologies, we proposed an image restoration algorithm for MRA-based pansharpening methods in this paper, which can be directly applied to the restoration of the fusion results without modifying the pansharpening methods. The contributions of the proposed restoration framework are as follows.

(1) We use the blind deblurring method based on the Tikhonov regular constraint model to estimate the blurring filter. The HPM scheme and the estimated filter are used to balance between spatial information injection and spectral information preservation of fusion results.

(2) A new restoration framework based on the IBP technique and enhanced images is constructed, and unlike the EBP method, the MTF-matched filter is replaced by the estimated filter in our proposed method. The reconstruction error is projected back to tune and update the estimated high-resolution MS images iteratively.

The rest of this paper is organized as follows. A short overview of MRA methods and our proposed image restoration method are provided in Section II. In Section III, experimental results based on real and degraded datasets are presented and analyzed. Finally, a conclusion is drawn in Section IV.

II. MATERIALS AND METHODS
A. SHORT OVERVIEW OF MRA METHODS
The basic principle of MRA-based method is to extract missing details of MS images from PAN images by multiscale decomposition, and then inject the details into MS images interpolated to the size of PAN to obtain high spatial resolution MS images $\widehat{MS}$. The MRA scheme is given by

$$\widehat{MS}_k = \widetilde{MS}_k + g_k \cdot D_k, \quad k = 1, \cdots, K \tag{1}$$

where $\widehat{MS}_k$ represents the fusion result, $\widetilde{MS}_k$ is the upsampled MS image, g_k indicates the injection gain matrix, subscript k denotes the k th band and K represents the number of MS bands. Detailed image D_k is defined as

$$D_k = P_k - P_k^{LP} \tag{2}$$

where P_k is the PAN image that is histogram-matched to $\widetilde{MS}_k$, and P_k^{LP} is the low-pass version of the PAN image. For MRA methods, different spectral channels may correspond to different P_k. Histogram matching of PAN images can be performed according to $\widetilde{MS}_k$ and the function P_k of k can be obtained [29]. In general, P_k^{LP} is calculated by iterative decomposition of MRA tools. Through the repeated applications of a multiscale analysis operator, a two-dimensional signal sequence with gradually reduced information is constructed [4]. It is the simplest method to calculate P_k^{LP} by linear time-invariant filter h_k

$$P_k^{LP} = P_k * h_k \tag{3}$$

where, $*$ denotes the convolution operation.

Calculation of the injection gain matrix can be divided into two categories of methods based on additive injection (HPF scheme) and methods based on multiplicative injection (HPM scheme) [4]. In this paper, the HPM scheme is used to enhance the spatial details of pansharpened images. The framework can be represented as

$$\widehat{MS}_k = \widetilde{MS}_k + \frac{\widetilde{MS}_k}{P_k^{LP}} \cdot (P_k - P_k^{LP}) = \widetilde{MS}_k \cdot \frac{P_k}{P_k^{LP}} \tag{4}$$

the ratio of MS image to low-resolution PAN image is used as a weighting coefficient for spatial details.

CS-based methods can effectively reduce spatial distortion, whereas MRA-based methods perform better in maintaining spectral characteristics. These two types of methods are complementary in terms of robustness of spatial and temporal deviations [19]. CS- and MRA-based injection frameworks have important differences in extracting details from PAN images. Since low-resolution PAN images with different surface objects cannot be well approximated according to the

weighted sum of selected MS bands based on CS methods, an MRA-based method is usually adopted to estimate the low-resolution version of the PAN.

The brief procedure of the MRA-based fusion method is as follows. First, the MS image is interpolated to the size of the PAN image, and then the low-pass version of the PAN image is obtained by the equivalent filter. R is the scale factor between the spatial resolution of the MS and PAN images. Different equivalent filters determine whether a downsampling operation is required. Finally, the injection gain coefficient is calculated, and the fusion result is generated by combining the extracted details with MS images.

B. BLURRING FILTER ESTIMATION
It is assumed that all MS bands are generated based on the same spatial degradation of the PAN images in the literature [22]. MS and PAN images can be regarded as blurred images and sharp images, respectively. First, a mathematical model of image degradation is established

$$g(x, y) = f(x, y) * h(x, y) + n(x, y) \tag{5}$$

where g and n are the degraded image and observation noise, respectively, f denotes the ideal sharp image; h represents the blurring filter, and $*$ is the convolution operator.

Images can usually be represented as matrices or vectors. The matrix-vector notation of (5) can be represented as

$$\mathbf{g} = \mathbf{fh} + \mathbf{n} \tag{6}$$

where $\mathbf{f} \in \mathbb{R}^{MN \times MN}$ is a matrix operator whose construction depends on the selection of boundary conditions of image $\mathbf{f}$ [30], and $M \times N$ denotes the image size. $\mathbf{h}$, $\mathbf{g}$ and $\mathbf{n}$ are represented by lexicographically ordering h, g and n, which belong to $\mathbb{R}^{MN}$.

The blurring filter can be estimated based on the application of the degradation model with the original PAN image and its equivalent low-pass version $\mathbf{P}_I$. Calculation of $\mathbf{P}_I$ by a linear combination of MS bands is as follows

$$\mathbf{P}_I = \sum_{i=1}^{K} \omega_i \widetilde{\mathbf{MS}}_i \tag{7}$$

where $\widetilde{\mathbf{MS}}$ is the MS image upsampled to the original PAN size, and $\boldsymbol{\omega} = [\omega_1, \omega_2, \ldots, \omega_K]$ denotes the weighting coefficient vector.

To estimate the blurring filter from the preprocessed equivalent PAN image, the optimization problem of minimizing the cost function as shown below needs to be solved

$$\underset{\mathbf{h}, \boldsymbol{\omega}}{\text{minimize}} \{ \|\mathbf{P}_I - \mathbf{Ph}\|^2 + \lambda \|\mathbf{h}\|^2 + \mu(\|\mathbf{D}_v\mathbf{h}\|^2 + \|\mathbf{D}_h\mathbf{h}\|^2) \}$$
$$\text{subject to } \mathbf{h}^T 1 = 1, \mathbf{h} \in \mathcal{H} \tag{8}$$

where regularization terms based on gradient operators are designed [31], which can also be regarded as prior information under the Bayesian framework [24]. According to the restoration model, the degraded image is fitted and restored. $\mathbf{D}_h, \mathbf{D}_v \in \mathbb{R}^{MN \times MN}$ are used to represent first-order

finite-difference operators in the horizontal and vertical, respectively. Constraints $\mathbf{h}^T\mathbf{1} = 1$ and $\mathbf{h} \in \mathcal{H}$ represent normalization and finite support, respectively, of the blurring filter. λ and μ are weights of regularization terms.

Equation (8) can also be represented as

$$f_{\mathbf{h}}(\mathbf{h}) = \underset{\mathbf{h},\boldsymbol{\omega}}{\text{minimize}}\{(\mathbf{P}_I - \mathbf{Ph})^T(\mathbf{P}_I - \mathbf{Ph}) + \lambda\mathbf{h}^T\mathbf{h}+$$
$$\mu((\mathbf{D}_v\mathbf{h})^T(\mathbf{D}_v\mathbf{h}) + (\mathbf{D}_h\mathbf{h})^T(\mathbf{D}_h\mathbf{h}))\} \quad (9)$$

as the quadratic form of the cost function, (9) is used to calculate the vector derivative of f with respect to $\mathbf{h}$. When following (10) is satisfied, a global minimum value can be obtained.

$$\partial f_{\mathbf{h}}(\mathbf{h})/\partial\mathbf{h}$$
$$= (\partial\{(\mathbf{P}_I - \mathbf{Ph})^T(\mathbf{P}_I - \mathbf{Ph}) + \lambda\mathbf{h}^T\mathbf{h}+$$
$$\mu((\mathbf{D}_v\mathbf{h})^T(\mathbf{D}_v\mathbf{h}) + (\mathbf{D}_h\mathbf{h})^T(\mathbf{D}_h\mathbf{h}))\})/\partial\mathbf{h} = 0$$
$$\Rightarrow 2\partial(\mathbf{P}_I - \mathbf{Ph})^T/\partial\mathbf{h} \cdot (\mathbf{P}_I - \mathbf{Ph}) + 2\lambda\mathbf{h}+$$
$$\mu(2\partial(\mathbf{D}_v\mathbf{h})^T/\partial\mathbf{h} \cdot (\mathbf{D}_v\mathbf{h}) + 2\partial(\mathbf{D}_h\mathbf{h})^T/\partial\mathbf{h} \cdot (\mathbf{D}_h\mathbf{h}))$$
$$= -2\mathbf{P}^T \cdot (\mathbf{P}_I - \mathbf{Ph}) + 2\lambda\mathbf{h} + 2\mu(\mathbf{D}_v^T\mathbf{D}_v\mathbf{h} + \mathbf{D}_h^T\mathbf{D}_h\mathbf{h})$$
$$= 2\mathbf{P}^T\mathbf{Ph} - 2\mathbf{P}^T\mathbf{P}_I + 2\lambda\mathbf{h} + 2\mu(\mathbf{D}_v^T\mathbf{D}_v\mathbf{h} + \mathbf{D}_h^T\mathbf{D}_h\mathbf{h}) = 0$$
$$(10)$$

Image and blur are not joint convex optimization, but when one variable is fixed, the equation is a convex optimization problem for the other variable, which can be solved by the strategy of alternative iterative optimization. This problem is transformed into a solution in which two convex optimization subproblems are performed alternatively. First, the coefficient $\boldsymbol{\omega}$ is estimated, then optimization of the blurring filter is performed. Calculating $\boldsymbol{\omega}$ with a given estimation of $\mathbf{h}$ finds the solution of simple least squares problems.

$$\widetilde{\mathbf{MS}}^T\boldsymbol{\omega} = \mathbf{Ph} \quad (11)$$

after calculating $\boldsymbol{\omega}$, estimation of $\mathbf{h}$ under a given $\boldsymbol{\omega}$ is as follows

$$[\mathbf{P}^T\mathbf{P} + \lambda\mathbf{I} + \mu\mathbf{D}_v^T\mathbf{D}_v + \mu\mathbf{D}_h^T\mathbf{D}_h]\mathbf{h} = \mathbf{P}^T\mathbf{P}_I$$
$$\Rightarrow \hat{\mathbf{h}} = [\mathbf{P}^T\mathbf{P} + \lambda\mathbf{I} + \mu\mathbf{D}_v^T\mathbf{D}_v + \mu\mathbf{D}_h^T\mathbf{D}_h]^{-1}\mathbf{P}^T\mathbf{P}_I \quad (12)$$

where $\hat{\mathbf{h}}$ represents the estimated blurring filter. During minimization of (8), it is necessary to perform multiple computations of the gradient of $f_{\mathbf{h}}(\mathbf{h})$, which is a time-consuming process, and the calculation can be accelerated by fast Fourier transform $\mathcal{F}\{\cdot\}$. The closed-form solution obtained by fast Fourier transform is as follows

$$\hat{\mathbf{h}} = \mathcal{F}^{-1}\left\{(\overline{\mathcal{F}\{\mathbf{P}\}} \circ \mathcal{F}\{\mathbf{P}_I\})/(\overline{\mathcal{F}\{\mathbf{P}\}} \circ \mathcal{F}\{\mathbf{P}\} + \lambda+\right.$$
$$\left.\mu(\overline{\mathcal{F}\{\mathbf{D}_h\}} \circ \mathcal{F}\{\mathbf{D}_h\} + \overline{\mathcal{F}\{\mathbf{D}_v\}} \circ \mathcal{F}\{\mathbf{D}_v\}))\right\} \quad (13)$$

where $\mathcal{F}\{\cdot\}$ and $\mathcal{F}^{-1}\{\cdot\}$ represent discrete Fourier transform and inverse Fourier transform, respectively, and $\overline{\mathcal{F}\{\cdot\}}$ denotes a complex conjugate of Fourier transform.

C. SPATIAL ENHANCEMENT

The restoration object in this paper is the pansharpened image obtained by the MRA method. Since the advantage of MRA tends to maintain the spectral information, the spatial details of the fusion results need to be enhanced before restoration. It has been proven through theory and practice that the histogram matching technique used as a preprocessing step pansharpening is effective for reducing spectral distortion [32], [33]. The HPM scheme is widely used in the spatial enhancement of fusion results [24], [26]. In the literature [22], a fusion model was defined by taking advantage of these two technologies, which can be called spatial enhancement (SE).

$\mathbf{P}_{LP}^{HM} \in \mathbb{R}^{K \times MN}$ denotes the low-resolution version of $\mathbf{P}^{HM}$. Generating $\mathbf{P}_{LP}^{HM}$ through a pyramid decomposition scheme is a widely used MRA method [34]. This process is usually accomplished by applying a smoothing low-pass linear filter, and the estimated blurring filter $\hat{\mathbf{h}}$ in the previous section is used in this part.

$$\mathbf{P}_{LP,k}^{HM} = \mathbf{P}_k^{HM} * \hat{\mathbf{h}} \quad (14)$$

where $\mathbf{P}^{HM} \in \mathbb{R}^{K \times MN}$ is the PAN image after histogram matching with the MS bands, aiming at compensating the radiation differences between the original MS and PAN images. $\mathbf{P}_k^{HM}$ can be calculated as follows

$$\mathbf{P}_k^{HM} = [\mathbf{P} - \mu_{\mathbf{p}}] \cdot \frac{\sigma_{\widetilde{\mathbf{MS}}_k}}{\sigma_P} + \mu_{\widetilde{\mathbf{MS}}_k} \quad (15)$$

where $\mu_{\mathbf{X}}$ denotes the mean of image $\mathbf{X}$, and $\sigma_{\mathbf{X}}$ denotes the standard deviation of image $\mathbf{X}$.

Based on the HPM scheme, spatial details of the PAN images are modulated into MS images with the ratio between the histogram-matched PAN images and low-pass PAN images to obtain fusion results $\{\widehat{\mathbf{MS}}_k^{spa}\}_{k=1,\cdots,K}$

$$\widehat{\mathbf{MS}}_k^{spa} = \widetilde{\mathbf{MS}}_k \cdot \frac{\mathbf{P}_k^{HM}}{\mathbf{P}_{LP,k}^{HM}} \quad (16)$$

where $\widehat{\mathbf{MS}} \in \mathbb{R}^{K \times MN}$, and the MS images are represented as two-dimensional matrices in which each column is a spectral vector of the corresponding pixel and each row represents a spectral band.

Fusion images obtained by MRA methods are represented as $\{\widehat{\mathbf{MS}}_k^{spe}\}_{k=1,\cdots,K}$, and fusion results after spatial enhancement are marked as $\{\widehat{\mathbf{MS}}_k^{fus}\}_{k=1,\cdots,K}$.

$$\widehat{\mathbf{MS}}_k^{fus} = (\widehat{\mathbf{MS}}_k^{spa} - \hat{\mathbf{h}} * \widehat{\mathbf{MS}}_k^{spa}) + \hat{\mathbf{h}} * \widehat{\mathbf{MS}}_k^{spe} \quad (17)$$

MRA and SE methods are combined to integrate the advantages of these two. $\widehat{\mathbf{MS}}_k^{spa} - \hat{\mathbf{h}} * \widehat{\mathbf{MS}}_k^{spa}$ denotes the spatial details extracted from the enhanced image $\widehat{\mathbf{MS}}_k^{spa}$ (see the Appendix for details). It can be concluded that $\hat{\mathbf{h}} * \widehat{\mathbf{MS}}_k^{spe}$ can extract efficient spectral information. A balance between these two methods is realized through the estimated blurring filter $\hat{\mathbf{h}}$, so that the spatial details of the fusion results obtained by the MRA methods can be enhanced while the spectral information is maintained well. The pseudocode for the spatial enhancement is summarized in Algorithm 1.

Algorithm 1 Spatial Enhancement Algorithm

Input: PAN and MS images, estimated blurring filter $\widehat{\mathbf{h}}$

Output: Spatially enhanced image $\widehat{\mathbf{MS}}_k^{\text{fus}}$

Begin

1   Interpolate MS image to PAN size to obtain $\widetilde{\mathbf{MS}}$

2   **for** $k = 1, \ldots, K$ **do**

3   Calculate histogram-matched PAN image
$$\mathbf{P}_k^{\text{HM}} = [\mathbf{P} - \mu_{P_k}] \cdot \frac{\sigma_{\widetilde{\mathbf{MS}}_k}}{\sigma_{P_k}} + \mu_{\widetilde{\mathbf{MS}}_k}$$

4   Perform SE method based on the HPM scheme
$$\widehat{\mathbf{MS}}_k^{\text{spa}} = \widetilde{\mathbf{MS}}_k \cdot \frac{\mathbf{P}_k^{\text{HM}}}{P_{\text{LP},\mathbf{k}}^{\text{HM}}}$$

5   Combine the MRA and SE methods
$$\widehat{\mathbf{MS}}_k^{\text{fus}} = (\widehat{\mathbf{MS}}_k^{\text{spa}} - \widehat{\mathbf{h}} * \widehat{\mathbf{MS}}_k^{\text{spa}}) + \widehat{\mathbf{h}} * \widehat{\mathbf{MS}}_k^{\text{spe}}$$

6   **end for**

7   Gather $\{\widehat{\mathbf{MS}}_k^{\text{fus}}\}_{k=1,\cdots,K}$ in $\widehat{\mathbf{MS}}^{\text{fus}}$

End

D. IMAGE RESTORATION BASED ON IBP

For the restoration of pansharpened images, the main degradation factors include downsampling and blurring. Assuming that the ideal high-resolution image is X, and the corresponding low-resolution image Y can be obtained by performing blurring and downsampling operations on X as follows

$$Y = (X * \mathcal{F}) \downarrow_r \tag{18}$$

where $\mathcal{F}$ represents the blurring filter of the imaging system, and the filter estimated by the blind deblurring method is used here, and $\downarrow_r$ denotes downsampling operator with scale factor r ($r = 4$ is usually found in pansharpening).

The IBP scheme [35] is a common method for solving the above model and has been successfully applied in superresolution literature [36], [37]. It was first proposed in [38] for pansharpening postprocessing. The reconstruction errors were projected and fused back to adjust the desired high-resolution images iteratively, which can effectively improve the spatial and spectral quality of pansharpening images.

The basic idea of the IBP algorithm is that, based on the input low-resolution image, the initial estimation of a high-resolution image $\hat{X}_0$ is given and projected to the low-resolution simulated image. The residual between the input low-resolution image and the analog low resolution image is the reconstruction error e, which is projected back to tune and update the desired high-resolution image $\hat{X}$ by iteration.

The reconstruction error e_t of the tth iteration can be calculated as follows

$$e_t = Y - (\hat{X}_t * \mathcal{F}) \downarrow_r \tag{19}$$

where t represents the t th iteration. Based on the reconstruction error obtained by (19), the estimation of high-resolution images is updated as follows

$$\hat{X}_{t+1} = \hat{X}_t + e_t \uparrow_r * \mathcal{G} \tag{20}$$

Algorithm 2 Image Restoration Based on IBP

Input: $\mathbf{MS}$, $\widehat{\mathbf{h}}$, spatially enhanced pansharpening image $\widehat{\mathbf{MS}}^{\text{fus}}$

Output: Restoration image $\widehat{\mathbf{MS}}$

Begin

1    $t = 0$, $t_{\max} = 100$, $\beta = 0.1$, $\widehat{\mathbf{MS}}_{k,0} = \widehat{\mathbf{MS}}^{\text{fus}}$

2   while $t < t_{\max}$

3   Perform blurring and downsampling operations
$$\overline{\mathbf{MS}}_{k,t} = \mathbf{MS} - (\widehat{\mathbf{MS}}_{k,t} * \widehat{\mathbf{h}}) \downarrow_r$$

4   Calculate the residual
$$e_{k,t}^{\text{MS}} = \mathbf{MS} - \overline{\mathbf{MS}}_{k,t}$$

5   Upsample and back project the residual
$$e_{\text{BP},t} = e_{k,t}^{\text{MS}} \uparrow_r * \widehat{\mathbf{h}}'$$

6   Update the estimated the high-resolution image
$$\widehat{\mathbf{MS}}_{k,t+1} = \widehat{\mathbf{MS}}_{k,t} + \beta e_{\text{BP},t}$$
where, β determines the floating range of pixel values

7    $\gamma_{t+1} = \text{norm}(\widehat{\mathbf{MS}}_{k,t+1} - \widehat{\mathbf{MS}}_{k,t})/\text{norm}(\widehat{\mathbf{MS}}_{k,t+1})$
where, $\text{norm}(\cdot)$ represents the matrix 2-norm

8   if $t > 3$

9   If the terminate condition of iteration is satisfied
$$|\gamma_{t-3} - \gamma_t| < 1e - 4$$

10   break;

11   end

12    $t = t + 1$

13   end while

End

---

where $\mathcal{G}$ denotes the back projection filter, $\mathcal{G} = \mathcal{F}^{-1}$; $\hat{X}_{t+1}$ and $\hat{X}_t$ are the estimated high resolution images in the $t + 1$th and tth iterations, respectively; $\uparrow$ represents the upsampling operator; r denotes the corresponding scale factor; and the residual is upsampled and back projected. Equations (19) and (20) are iteratively performed until a sufficiently small difference between the input low-resolution image and the analog image is achieved.

The literatures [39] and [40] provide the conditions for the convergence of the above equations to the desired image. The updating rules of (19) and (20) can converge to a desired high-resolution image under the condition that (18) is satisfied and $\|\delta - \mathcal{F} * \mathcal{G} \downarrow_r\|_2 < 1$ (δ represents a unit pulse function centered at $(0, 0)$, $\delta = ((Y - X * \mathcal{F}) \downarrow_r) \uparrow_r)$.

$$
\begin{aligned}
e_{t+1} &= Y - (\hat{X}_{t+1} * \mathcal{F}) \downarrow_r \\
&= Y - ((\hat{X}_t + (Y - (\hat{X}_t * \mathcal{F}) \downarrow_r) \uparrow_r * \mathcal{G}) * \mathcal{F} \downarrow_r \\
&= Y - (\hat{X}_t * \mathcal{F}) \downarrow_r - (Y - (\hat{X}_t * \mathcal{F}) \downarrow_r) \uparrow_r * \mathcal{G} * \mathcal{F} \downarrow_r \\
&= (Y - (\hat{X}_t * \mathcal{F}) \downarrow_r) * (\delta - \mathcal{G} * \mathcal{F} \downarrow_r) \\
&= e_t * (\delta - \mathcal{G} * \mathcal{F} \downarrow_r) \tag{21}
\end{aligned}
$$

since $\|e_{t+1}\|_2 = \|e_t * (\delta - \mathcal{G} * \mathcal{F} \downarrow_r)\|_2 \leq \|e_t\|_2 * \|\delta - \mathcal{G} * \mathcal{F} \downarrow_r\|_2$, the limit formula can be obtained: $\lim_{t\to\infty} (\hat{X}_t * \mathcal{F}) \downarrow_r = Y$. According to the formula derivation, it is proven that the residual is attenuated during each iteration, and the error on low-resolution images tends to 0. IBP-based
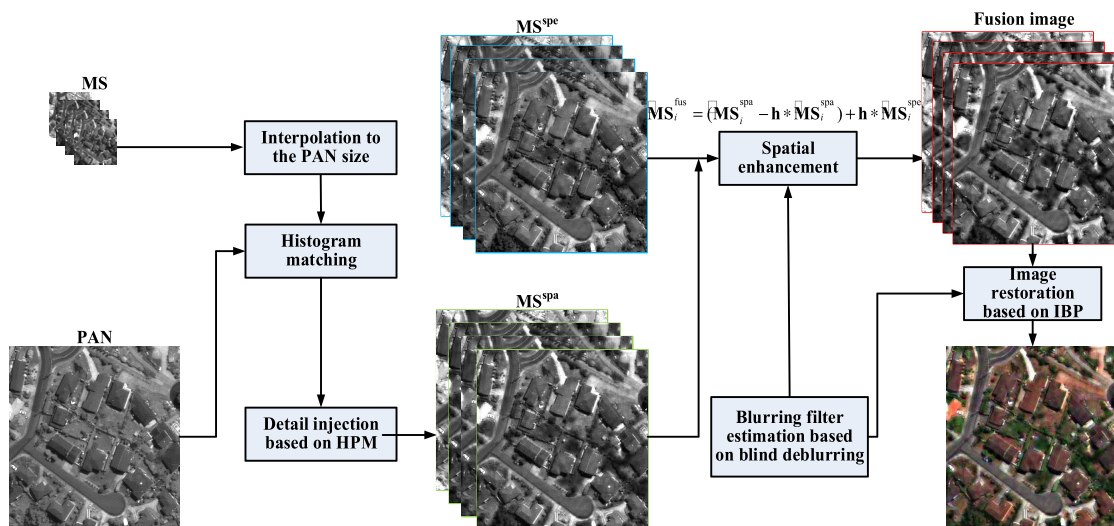
FIGURE 1. The flow chart of the proposed restoration method.
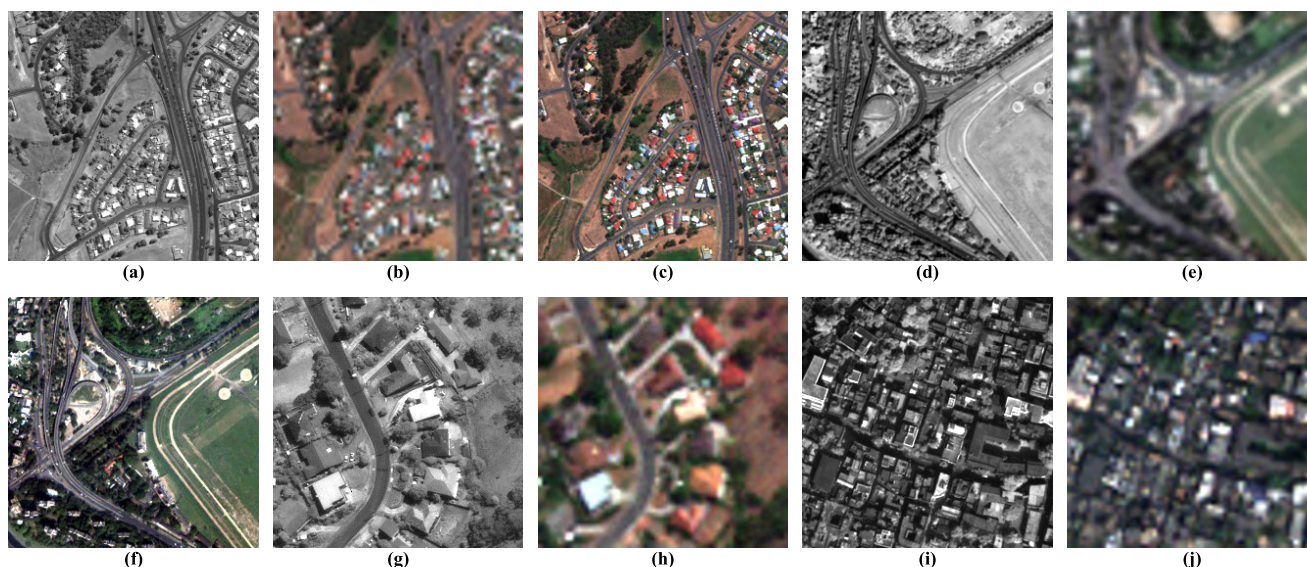

FIGURE 2. Experimental images on the degraded and real data (images in (a–f) came from the GeoEye-1 satellite, and the images in (g–j) came from the QuickBird satellite): (a) degraded PAN image 1; (b) degraded MS image 1; (c) reference image 1; (d) degraded PAN image 2; (e) degraded MS image 2; (f) reference image 2; (g) real PAN image 1; (h) real MS image 1; (i) real PAN image 2; (j) real MS image 2.

restoration can be summarized as Algorithm 2. The flow chart of the proposed restoration method is illustrated in Fig. 1.

III. EXPERIMENTS AND RESULTS

This section is divided into three parts. In the first part, the data sets and pansharpening methods used in the experiment are introduced. In the second part, the quantitative evaluation indices adopted in this paper are briefly discussed. The third part is the experimental analysis and discussion based on real and degraded data sets.

A. DATA SETS AND PANSHARPENING METHODS

In the experiment, two data sets from the QuickBird and GeoEye-1 satellites are selected for experimental verification of the proposed method, as shown in Fig. 2. The data

set from the GeoEye-1 satellite was captured in Hobart, Australia, on 24 February 2009. The spatial resolution of the MS and PAN images was 2 m and 0.5 m, respectively. The QuickBird dataset was captured on 21 November 2002 from National Forest Park in Sundarbans, India. The MS and PAN images have spatial resolutions of 2.8 m and 0.7 m, respectively. The datasets used in this paper consist of one PAN channel and four MS channels (red(R), green(G), blue(B) and near-infrared (NIR)). The MS and fused MS images shown in the figures are displayed by three channels, R, G and B. In the experiment, due to the lack of reference images for performance evaluation, the source images are processed by MTF filtering with a downsampling factor of 4, and the original MS images are taken as reference images. The sizes of the PAN and MS images used in this paper are

256×256 and 64×64, respectively, and the reference image size is 256×256.

The implementations of the tested pansharpening methods are from the pansharpening MATLAB toolbox released by Vivone, which is published together with a review of CS and MRA methods [4]. The toolbox covers several state-of-the-art pansharpening methods. The following eight fusion methods based on MRA are used to validate the restoration method proposed in this paper, including HPF [12], SFIM [13], ATWT [11], AWLP [10], MTF-GLP with HPM (MTF-GLP-HPM) [41], MTF-GLP with context-based decision (MTF-GLP-CBD) [42], morphological filter and half gradients (MF-HG) [43] and filter estimation and HPM (FE-HPM) [22]. The first six methods are from the toolbox. MF-HG was proposed by Restaino *et al.* in 2016, and FE-HPM was proposed by Vivone *et al.* in 2015. The available codes for these two pansharpening methods can be found at "http://openremotesensing.net/." Parameter settings for the above eight pansharpening methods are based on the authors' discussions in their papers.

Degraded and real data sets are used for experimental analysis to discuss whether the fusion quality of the images obtained by the eight MRA methods improves with restoration to prove the effectiveness of the proposed restoration method in this paper. A comparison of restored pansharpening results based on EBP and the proposed method is given, and the gains obtained in the percentage of evaluation indices by postrestoration methods are shown.

Eight MRA methods selected in the experimental part are briefly summarized in Table 1, which provide a basis for the filtering framework and injection gain in Equation (1). For a detailed overview, please refer to the literature [4].

B. QUALITY INDICES

The quality evaluation of pansharpening mainly aims at two aspects: the injection of spatial details, which mainly evaluates the spatial quality of fused images, and the preservation of spectral information, which mainly measures the maintenance of original spectral properties. The existing evaluation methods of pansharpening include objective and subjective evaluations. The subjective evaluation method is relatively simple and intuitive, but it has certain subjectivity and one-sidedness due to the influence of a variety of human factors. Therefore, subjective evaluation is only used as an auxiliary method to measure the fusion quality. It is necessary to select some reliable objective evaluation indices to perform quantification analysis. Objective evaluation is a challenging problem because there is no reference image in practical application. At present, there are two methods for quantitatively evaluating the fusion results. One method performs an evaluation on reduced resolution based on the scale invariance assumption according to Wald's protocol [27]. The other method performs a full resolution evaluation without reference images.

1) REDUCED RESOLUTION EVALUATION

According to Wald's protocol, fusion images should be as similar as possible to high-resolution images collected by MS sensors in which the spatial resolution is the same as the PAN images. However, this cannot be obviously verified in practice. Therefore, source images for pansharpening are obtained by reducing the resolution of original images, and original MS images are taken as corresponding reference images. Three indices are utilized for the degraded datasets, including relative dimensionless global error in synthesis (ERGAS) [44], spectral angle mapper (SAM) [45] and Q4 [46]. The ideal values of ERGAS and SAM are 0, and for Q4, the ideal value is 1.

2) FULL RESOLUTION EVALUATION

For the evaluation of full resolution image fusion, quantitative indices are usually designed by analyzing the relationship between fusion results and original images. The most commonly used evaluation index is the quality with no reference (QNR) [47], which includes two independent indices: the spectral distortion D_λ and the spatial distortion D_s. A larger value of QNR indicates better fusion quality, while the opposite is true for D_λ and D_s.

C. ANALYSIS OF EXPERIMENTAL RESULTS

The display of result images includes the fused images obtained by the eight MRA-based pansharpening methods and the images after restoration based on EBP and the pro-

TABLE 1. Overview of MRA-based pansharpening methods.

Methods	MRA Type and Filter	Injection Gain
High-Pass Filtering (HPF) [12]	ATWT; Box filter	1
Smoothing Filter-Based Intensity Modulation (SFIM) [13]	ATWT; Box filter	$\widetilde{\mathrm{MS}}_k \, / \, P^{\mathrm{LP}}$
A Trous Wavelet Transform (ATWT) [11]	ATWT; Starck and Murtagh (S&M) filter	1
Additive Wavelet Luminance Proportional (AWLP) [10]	ATWT; S&M filter	$\widetilde{\mathrm{MS}}_k \, / \, \dfrac{1}{N} \displaystyle\sum_{k=1}^{K} \widetilde{\mathrm{MS}}_k$
Generalized Laplacian Pyramid with Modulation Transfer Function (MTF-GLP) [14]	GLP; MTF filter	1
MTF-GLP with High-Pass Modulation (MTF-GLP-HPM) [41]	GLP; MTF filter	$\widetilde{\mathrm{MS}}_k \, / \, P^{\mathrm{LP}}$
MTF-GLP with Context Based Decision (MTF-GLP-CBD) [42]	GLP; MTF filter	$\mathrm{cov}(P^{\mathrm{LP}}, \widetilde{\mathrm{MS}}_k) \, / \, \mathrm{var}(P^{\mathrm{LP}})$
Morphological Filter and Half Gradients (MF-HG) [43]	HG; Morphological filter	$\widetilde{\mathrm{MS}}_k \, / \, P^{\mathrm{LP}}$

TABLE 2. Results for the fusion images in figure 3 at reduced scale.

Method	ERGAS			SAM			Q4		
	fuse	restore	change(%)	fuse	restore	change(%)	fuse	restore	change(%)
HPF	4.0312	4.2037	-4.2791	5.9025	5.8520	0.8556	0.8901	0.8920	0.2135
		3.8646	4.1328		5.4529	7.6171		0.9030	1.4493
SFIM	3.9369	4.1486	-5.3773	5.6704	5.4651	3.6206	0.8948	0.8950	0.0224
		3.8768	1.5266		5.4567	3.7687		0.9028	0.8941
ATWT	3.9920	4.2628	-6.7836	6.0425	6.0143	0.4667	0.8956	0.8914	-0.4690
		3.8901	2.5526		5.4883	9.1717		0.9028	0.8039
AWLP	3.9687	4.2446	-6.9519	5.6611	5.5291	2.3317	0.8990	0.8941	-0.5451
		3.8958	1.8369		5.4408	3.8915		0.9027	0.4116
MTF-GLP-HPM	3.8806	4.2253	-8.8826	5.7356	5.5017	4.0780	0.9004	0.8938	-0.7330
		3.9089	-0.7293		5.4878	4.3204		0.9024	0.2221
MTF-GLP-CBD	6.8347	6.8074	0.3994	8.8873	8.7959	1.0284	0.7985	0.8044	0.7389
		4.1722	38.9556		5.7875	34.8790		0.8955	12.1478
Method	ERGAS			SAM			Q4		
	fuse	restore	change(%)	fuse	restore	change(%)	fuse	restore	change(%)
MF-HG	4.1183	4.2434	-3.0377	5.7723	5.5068	4.5996	0.8911	0.8937	0.2918
		3.9609	3.8220		5.5398	4.0279		0.9014	1.1559
FE-HPM	3.8168	4.1388	-8.4364	5.7048	5.4905	3.7565	0.9013	0.8961	-0.5769
		3.8918	-1.9650		5.4716	4.0878		0.9025	0.1331

TABLE 3. Results for the fusion images in figure 4 at reduced scale.

Method	ERGAS			SAM			Q4		
	fuse	restore	change(%)	fuse	restore	change(%)	fuse	restore	change(%)
HPF	7.5681	7.7032	-1.7851	9.9056	9.6935	2.1412	0.6391	0.6464	1.1422
		7.3718	2.5938		9.6628	2.4511		0.6837	6.9786
SFIM	7.5248	7.6456	-1.6054	9.6728	9.5369	1.4050	0.6560	0.6578	0.2744
		7.4104	1.5203		9.6818	-0.0930		0.6850	4.4207
ATWT	7.3728	7.5475	-2.3695	10.0243	9.7628	2.6087	0.6641	0.6622	-0.2861
		7.3415	0.4245		9.6620	3.6142		0.6876	3.5386
AWLP	7.2390	7.4668	-3.1468	9.4281	9.3195	1.1519	0.6764	0.6707	-0.8427
		7.3268	-1.2129		9.5949	-1.7692		0.6890	1.8628
MTF-GLP-HPM	7.2988	7.5753	-3.7883	9.6338	9.5673	0.6903	0.6828	0.6714	-1.6696
		7.3669	-0.9330		9.6548	-0.2180		0.6893	0.9520
MTF-GLP-CBD	7.9073	8.1552	-3.1351	10.3169	10.3030	0.1347	0.6627	0.6521	-1.5995
		7.3168	7.4678		9.5978	6.9701		0.6910	4.2704
MF-HG	7.2356	7.4188	-2.5319	9.7046	9.5414	1.6817	0.6893	0.6811	-1.1896
		7.3535	-1.6294		9.6682	0.3751		0.6912	0.2756
FE-HPM	7.1422	7.4020	-3.6375	9.7051	9.5271	1.8341	0.6995	0.6838	-2.2445
		7.1634	0.2968		9.6344	0.7285		0.6997	0.0286

posed method. To facilitate a subjective visual comparison, the MS images in the figures are shown in RGB colors. The results of corresponding objective indices are summarized in Table 2–Table 5. Columns in tables are grouped according to different quality indices, and each group is divided into three columns. The column marked "fuse" denotes the fusion result obtained by each MRA method. The column labeled "restore" is the result with the restoration postprocessing. The column "change (%)" shows the gain percentage of the corresponding evaluation index; a positive value represents an improvement of the corresponding index after restoration, while the negative value indicates a degradation of the index.

Note that the results with EBP as the restoration method are shown in green, and results with the proposed method as postprocessing are represented in blue.

1) EXPERIMENTAL RESULTS ON DEGRADED DATA

The pansharpening results of eight MRA-based methods with and without restoration based on the degraded GeoEye-1 dataset are shown in Fig. 3. The figures without dotted borders present the pansharpening results, and the restoration results based on EBP and our proposed method are shown in dotted borders in different colors. Green indicates EBP, and blue indicates our proposed method. Image results obtained

TABLE 4. Results for the fusion images in figure 5 at full scale.

Method	D_λ			D_s			QNR		
	fuse	restore	change(%)	fuse	restore	change(%)	fuse	restore	change(%)
HPF	0.1562	0.1394	10.7554	0.0552	0.0818	-48.1884	0.7972	0.7902	-0.8780
		0.1432	8.3227		0.0734	-32.9710		0.7939	-0.4140
SFIM	0.1505	0.1478	1.7940	0.0542	0.0828	-52.7675	0.8035	0.7816	-2.7256
		0.1467	2.5249		0.0841	-55.1661		0.7815	-2.7380
ATWT	0.1775	0.1443	18.7042	0.0730	0.0765	-4.7945	0.7624	0.7902	3.6464
		0.1464	17.5211		0.0713	2.3288		0.7928	3.9874
AWLP	0.1733	0.1583	8.6555	0.0644	0.0855	-32.7640	0.7735	0.7697	-0.4913
		0.1473	15.0029		0.0734	-13.9752		0.7901	2.1461
MTF-GLP-HPM	0.1769	0.1504	14.9802	0.0680	0.0877	-28.9706	0.7672	0.7751	1.0297
		0.1462	17.3544		0.0716	-5.2941		0.7927	3.3238
MTF-GLP-CBD	0.2084	0.1875	10.0288	0.0600	0.0779	-29.8333	0.7441	0.7492	0.6854
		0.1507	27.6871		0.0698	-16.3333		0.7900	6.1685
MF-HG	0.1871	0.1501	19.7755	0.0753	0.0830	-10.2258	0.7516	0.7793	3.6855
		0.1470	21.4324		0.0718	4.6481		0.7917	5.3353
FE-HPM	0.1906	0.1465	23.1375	0.0764	0.0806	-5.4974	0.7475	0.7847	4.9766
		0.1492	21.7209		0.0688	9.9476		0.7922	5.9799

TABLE 5. Results for the fusion images in figure 6 at full scale.

Method	D_λ			D_s			QNR		
	fuse	restore	change(%)	fuse	restore	change(%)	fuse	restore	change(%)
HPF	0.0677	0.0594	12.2600	0.0371	0.0111	70.0809	0.8977	0.9301	3.6092
		0.0583	13.8848		0.0199	46.3612		0.9230	2.8183
SFIM	0.0550	0.0575	-4.5455	0.0235	0.0049	79.1489	0.9228	0.9379	1.6363
		0.0572	-4.0000		0.0188	20.0000		0.9251	0.2492
ATWT	0.0854	0.0633	25.8782	0.0688	0.0241	64.9710	0.8516	0.9141	7.3391
		0.0603	29.3911		0.0243	64.6802		0.9169	7.6679
AWLP	0.0664	0.0622	6.3253	0.0553	0.0141	74.5037	0.8820	0.9246	4.8299
		0.0583	12.1988		0.0232	58.0470		0.9198	4.2857
MTF-GLP-HPM	0.0699	0.0614	12.1602	0.0561	0.0212	62.2103	0.8779	0.9187	4.6475
		0.0587	16.0229		0.0225	59.8930		0.9201	4.8069
MTF-GLP-CBD	0.0785	0.0613	21.9108	0.0500	0.0262	47.6000	0.8754	0.9140	4.4094
		0.0605	22.9299		0.0231	53.8000		0.9178	4.8435
MF-HG	0.0807	0.0604	25.1549	0.0587	0.0252	57.0698	0.8653	0.9160	5.8592
		0.0597	26.0223		0.0215	63.3731		0.9201	6.3331
FE-HPM	0.0764	0.0613	19.7644	0.0641	0.0213	66.7707	0.8644	0.9187	6.2818
		0.0595	22.1204		0.0257	59.9064		0.9164	6.0157

by restoration methods are prefixed with ''restored'' before their names. EBP adds ''1'' at the end of the name, and the proposed method adds ''2''. Compared with the fused images obtained by the eight MRA methods, it can be seen that the spectral quality of the restored image with the EBP method has improved to some extent, but some distortion is caused by excessive enhancement of spatial details and high contrast in local areas; in contrast, most of the results based on the proposed method have significantly improved, with clearer spatial details and better spectral information. To summarize, the subjective visual effects demonstrate that the proposed method effectively improves the quality of the fusion results, preserving clear edges and showing natural colors.

Table 2 shows the evaluation results for the GeoEye-1 dataset obtained by the eight pansharpening methods with and without restoration by EBP and the proposed method at reduced resolution. According to the table, it can be seen that in the evaluation results of EBP, except for the improvement in the ERGAS index of the MTF-GLP-CBD method after restoration, the index gains of the other methods are all negative, which indicates that the EBP method suffers spatial distortion in most restoration results. This is due to the introduction of excessive spatial details in the design of the method. The SAM index of the restored images based on EBP improved compared with that before restoration. In addition, relative changes in the SAM score of

FIGURE 3. Fusion images with and without restoration on the GeoEye-1 data set at reduced scale: (a) HPF; (b) SFIM; (c) ATWT; (d) AWLP; (e) restored HPF 1; (f) restored SFIM 1; (g) restored ATWT 1; (h) restored AWLP 1; (i) restored HPF 2; (j) restored SFIM 2; (k) restored ATWT 2; (l) restored AWLP 2; (m) MTF-GLP-HPM; (n) MTF-GLP-CBD; (o) MF-HG; (p) FE-HPM; (q) restored MTF-GLP-HPM 1; (r) restored MTF-GLP-CBD 1; (s) restored MF-HG 1; (t) restored FE-HPM 1; (u) restored MTF-GLP-HPM 2; (v) restored MTF-GLP-CBD 2; (w) restored MF-HG 2; (x) restored FE-HPM 2.

MF-HG are better than those of the proposed method, with an increase of 4.5996%. The Q4 indices obtained by HPF, SFIM, MTF-GLP-CBD and MF-HG exhibit positive gains after restoration, while the indices in ATWT, AWLP, MTF-GLP-HPM and FE-HPM decreased, showing a decrement of 0.4690%, 0.5451%, 0.7330% and 0.5769%, respectively, which is small. For the proposed method, we can see that all the MRA methods except for MTF-GLP-HPM and FE-HPM show significant improvement using the proposed method. In particular, the restored result obtained by MTF-GLP-CBD shows the greatest improvement compared with those of the other methods with improvements of 38.9556%, 34.8790% and 12.1478% for the ERGAS, SAM and Q4 indices, respectively.

Fig. 4 shows the fusion results on the QuickBird dataset at reduced resolution for the MRA methods with and without restoration. It is apparent that the spectral quality is enhanced based on the EBP method, but the spatial quality is relatively poor, especially for the MTF-GLP-HPM and MTF-GLP-CBD methods. The spatial distortion may be caused by excessive detail injection. In contrast, we can see that most of the restored images based on the proposed method are improved in visual effect. As seen in Fig. 4 (i), the fusion result of HPF looks more detailed after restoration, and the fusion result obtained by MTF-GLP-CBD with restoration can obtain rational details and natural colors, as shown in Fig. 4 (v). For the other methods, it can be seen that the restored images obtained by using the proposed method look more detailed with fewer artifacts, and achieve more similar colors to the reference images. From the perspective of subjective visual effect, the restored images based on the proposed method are obviously better than that based on EBP.

The statistical results of the eight pansharpening methods evaluated at reduced resolution based on the QuickBird dataset are illustrated in Table 3. The results of EBP show that the relative changes in the ERGAS score of all methods are negative, and only HPF and SFIM methods show gains in the Q4 metric, with an improvement of 1.1422% and 0.2744%, respectively. The restored results obtained by EBP achieve a relatively better SAM. The largest gains are shown by the SFIM, AWLP, MTF-GLP-HPM, MF-HG and FE-HPM methods. From the results of the proposed method, it can be seen that every MRA method shown gains in Q4 index after restoration. The SAM indices of the restored images obtained by the methods except for SFIM, AWLP and MTF-GLP-HPM have improved, and the relative changes in the ERGAS scores of most methods are positive. Most improved indices are from the restoration results of the MTF-GLP-CBD method, which have an improvement of 7.4678%, 6.9701% and 4.2704% for the ERGAS, SAM and Q4 indices, respectively.

2) EXPERIMENTAL RESULTS ON REAL DATA

Fig. 5 shows the fusion results of each MRA method with and without restoration based on the GeoEye-1 dataset at full resolution. Restored images obtained by EBP look more realistic in brightness and hue but have relatively poor spatial quality. For example, the SFIM method introduces some artifacts and noise in the fusion results, resulting in obvious spatial distortion in local areas, as shown in Fig. 5 (f). For our proposed method, it can be seen that the image quality after restoration significantly improves, with clearer spatial details and brighter colors, showing better visual effects. Compared with the fused images without restoration, local spatial distortion appears in the fusion results obtained by the HPF and SFIM methods after restoration. Some spatial details are lost after restoration for the MTF-GLP-CBD method, and visually, the details of the fusion results without restoration are clearer and sharper. In general, restored images obtained by our proposed method show a better visual effect than the EBP method.

The evaluation results of the D_λ, D_s and QNR indices based on real datasets from the GeoEye-1 satellite are summarized in Table 4. It can be seen that the restored images obtained by the EBP method show gains in the D_λ metric, and the largest gains are obtained by the HPF, ATWT and FE-HPM methods compared to those using the proposed method, with an increase of 10.7554%, 18.7042% and 23.1375%, respectively. However, the D_s index exhibits negative gains in all methods after restoration. Most MRA methods show improvement in the QNR index, and only HPF, SFIM and AWLP have negative gains, with decreases of 0.8780%, 2.7256% and 0.4913%, respectively. Compared with the EBP method, most of the D_λ from the restored results obtained by the proposed method are superior. The relative changes in the D_s score of the ATWT, MF-HG and FE-HPM methods are positive. For the QNR index, all MRA methods except HPF and SFIM benefit from the restoration. In conclusion, most MRA methods show improvements using the proposed restoration method, particularly the FE-HPM method, and the increased rates of the D_λ, D_s and QNR indices are 21.7209%, 9.9476% and 5.9799%, respectively.

The pansharpening results with and without restoration based on the QuickBird dataset at full resolution are shown in Fig. 6. From the perspective of visual effects, restored images obtained by EBP and the proposed method look more detailed and have better color balance. However, comparatively, the proposed method gives a more natural visual effect, similar to the SFIM and AWLP methods, which acquire an obvious effect. These methods cannot achieve a good visual effect when restored by EBP; the tones seem lighter, and the details are excessively enhanced in local areas.

Table 5 shows the results of the evaluation indices for the QuickBird satellite datasets at full resolution. As seen from the table, all the restored results obtained by EBP and our proposed method show improvements in the D_s and QNR indices. For the D_λ index, all pansharpening methods except for SFIM benefit from the restoration. In addition, all methods achieve better D_λ and QNR with our proposed method, aside from the HPF, SFIM and AWLP methods, which show worse effect in QNR. However, the EBP method outperforms
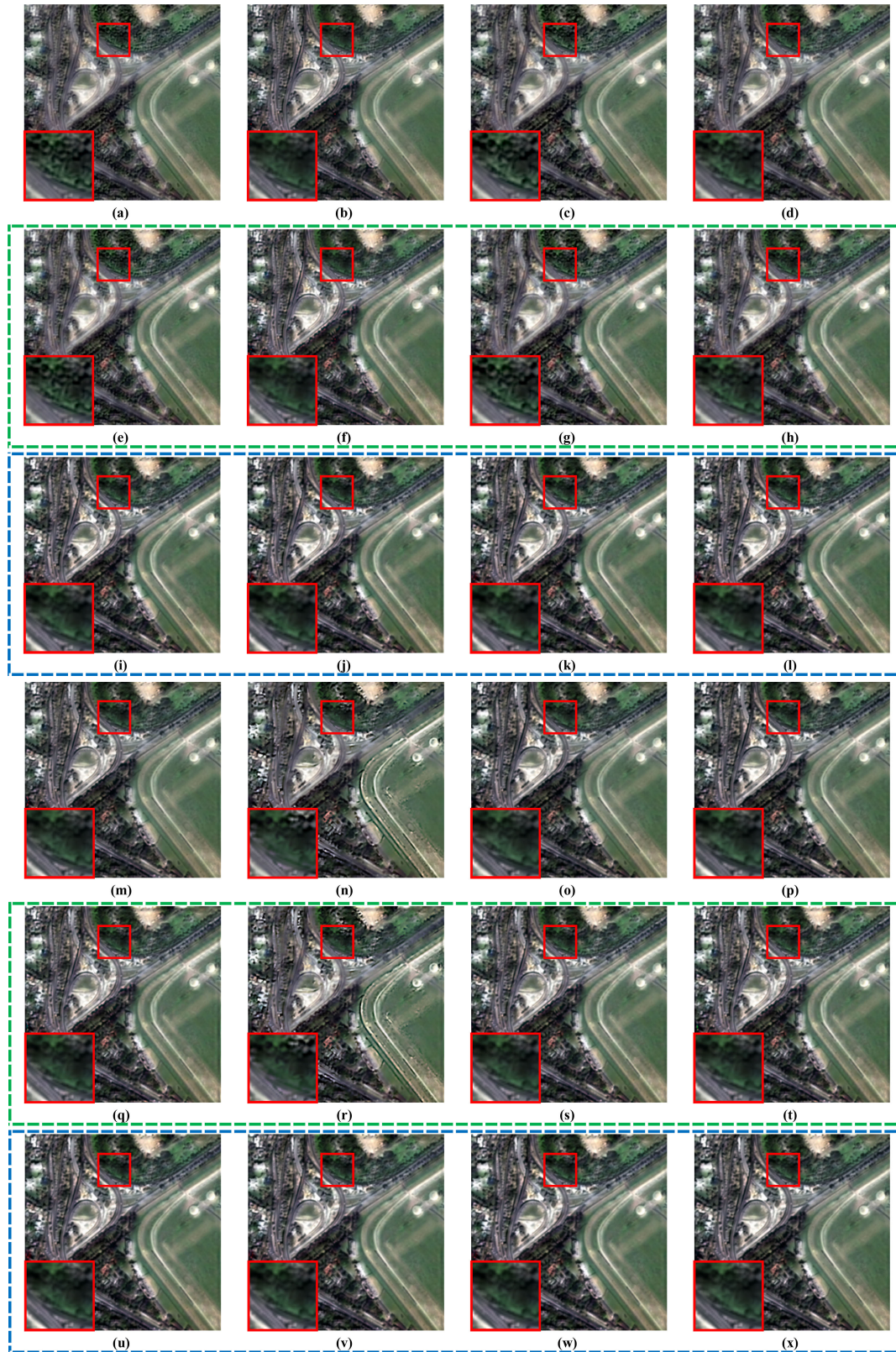
FIGURE 4. Fusion images with and without restoration on the QuickBird data set at reduced scale: (a) HPF; (b) SFIM; (c) ATWT; (d) AWLP; (e) restored HPF 1; (f) restored SFIM 1; (g) restored ATWT 1; (h) restored AWLP 1; (i) restored HPF 2; (j) restored SFIM 2; (k) restored ATWT 2; (l) restored AWLP 2; (m) MTF-GLP-HPM; (n) MTF-GLP-CBD; (o) MF-HG; (p) FE-HPM; (q) restored MTF-GLP-HPM 1; (r) restored MTF-GLP-CBD 1; (s) restored MF-HG 1; (t) restored FE-HPM 1; (u) restored MTF-GLP-HPM 2; (v) restored MTF-GLP-CBD 2; (w) restored MF-HG 2; (x) restored FE-HPM 2.

FIGURE 5. Fusion images with and without restoration on the GeoEye-1 data set at full scale: (a) HPF; (b) SFIM; (c) ATWT; (d) AWLP; (e) restored HPF 1; (f) restored SFIM 1; (g) restored ATWT 1; (h) restored AWLP 1; (i) restored HPF 2; (j) restored SFIM 2; (k) restored ATWT 2; (l) restored AWLP 2; (m) MTF-GLP-HPM; (n) MTF-GLP-CBD; (o) MF-HG; (p) FE-HPM; (q) restored MTF-GLP-HPM 1; (r) restored MTF-GLP-CBD 1; (s) restored MF-HG 1; (t) restored FE-HPM 1; (u) restored MTF-GLP-HPM 2; (v) restored MTF-GLP-CBD 2; (w) restored MF-HG 2; (x) restored FE-HPM 2.

FIGURE 6. Fusion images with and without restoration on the QuickBird data set at full scale: (a) HPF; (b) SFIM; (c) ATWT; (d) AWLP; (e) restored HPF 1; (f) restored SFIM 1; (g) restored ATWT 1; (h) restored AWLP 1; (i) restored HPF 2; (j) restored SFIM 2; (k) restored ATWT 2; (l) restored AWLP 2; (m) MTF-GLP-HPM; (n) MTF-GLP-CBD; (o) MF-HG; (p) FE-HPM; (q) restored MTF-GLP-HPM 1; (r) restored MTF-GLP-CBD 1; (s) restored MF-HG 1; (t) restored FE-HPM 1; (u) restored MTF-GLP-HPM 2; (v) restored MTF-GLP-CBD 2; (w) restored MF-HG 2; (x) restored FE-HPM 2.

TABLE 6. Time costs of different fusion methods with and without restoration.

Size of fusion image	MRA Method		Restoration method	
			EBP	Proposed
	HPF	0.0242	1.8082	4.1734
	SFIM	0.0350	1.9027	4.2614
	ATWT	0.1347	1.9134	5.0906
Time consuming (s) 256×256	AWLP	0.1006	1.8961	5.0672
	MTF-GLP-HPM	0.1636	1.9315	5.1589
	MTF-GLP-CBD	34.6494	36.5246	39.1023
	MF-HG	0.3194	1.8740	5.7131
	FE-HPM	1.3200	4.9702	7.2832

our proposed method in terms of D_s obtained by most MRA methods. Therefore, the whole effect of the proposed method is better than the EBP method.

3) COMPUTATIONAL COMPLEXITY

Table 6 shows the time complexity of the eight MRA methods with and without restoration. The size of the fused images is 256×256 pixels, so the average running times are calculated based on each dataset. As seen from the table, pansharpening based on MRA has relatively good time performance, and the time increases with the restoration process. We can see the calculation time of the MTF-GLP-CBD method is higher than the other pansharpening methods, and restoration based on the proposed method costs more time than the EBP method. The percentages of time gain after restoration with the proposed method and EBP the method are 12.8513% and 5.4119%, respectively. For the HPF method with a shorter fusion time, the time increases by 4.1492 s and 1.7840 s for our proposed method and the EBP method. Obviously, the restoration postprocessing has a relatively large impact on the fusion methods. Therefore, optimizations of postprocessing is a question for further study.

IV. CONCLUSION

The MRA-based pansharpening methods are simple, fast and efficient, with excellent spectral preservation ability. However, the spatial details of the fusion results may be less than ideal, and there are ringing artifacts caused by the methods or images. Based on this, an image restoration method for MRA methods is proposed in this paper. Based on estimating the relationship between the original MS and PAN images, the blurring filter can be obtained, which is applied to balance the detail injection and the spectral preservation of pansharpening results, and then the enhanced fusion results are tuned and optimized by the back-projection of iterative errors based on the IBP method. Based on eight state-of-the-art MRA methods, datasets from the GeoEye-1 and QuickBird satellites are used to analyze the restoration method at reduced and full scale. The experimental results show that the proposed method can significantly improve the fusion quality for most MRA methods.

The improvement in pansharpening quality mainly depends on the implementation of the restoration method.

Considering the subjective visual effect, most restored images achieve improvement of spatial and spectral quality.

Most of the MRA methods obtain clearer images by the restoration method proposed in this paper, which contains more detailed information and reduces ringing artifacts to some extent. For colorful source images, fusion results of some MRA methods show a decrease in spatial quality after restoration. This is because the MRA methods have great advantages in spectral maintenance, which is more apparent when the restoration is applied to color-rich images. Therefore, after iterative restoration based on IBP, although the spectral quality improves, it also creates distortion in the spatial details to some extent. However, in general, whether the subjective visual effect or objective evaluation indices, the quality of restored images improves.

In the next step, we plan to study the adaptive enhancement of spatial details based on the evaluation of spectral preservation to avoid the imbalance between the spatial and spectral information caused by excessive injection of spatial details or spectral information.

REFERENCES

[1] G. A. Shaw and H.-H. K. Burke, "Spectral imaging for remote sensing," *Lincoln Lab. J.*, vol. 14, no. 1, pp. 3–28, 2003.

[2] S. Li, X. Kang, L. Fang, J. Hu, and H. Yin, "Pixel-level image fusion: A survey of the state of the art," *Inf. Fusion*, vol. 33, pp. 100–112, Jan. 2017.

[3] C. Thomas, T. Ranchin, L. Wald, and J. Chanussot, "Synthesis of multispectral images to high spatial resolution: A critical review of fusion methods based on remote sensing physics," *IEEE Trans. Geosci. Remote Sens.*, vol. 46, no. 5, pp. 1301–1312, May 2008.

[4] G. Vivone, L. Alparone, J. Chanussot, M. D. Mura, A. Garzelli, G. A. Licciardi, R. Restaino, and L. Wald, "A critical comparison among pansharpening algorithms," *IEEE Trans. Geosci. Remote Sens.*, vol. 53, no. 5, pp. 2565–2586, May 2015.

[5] W. J. Carper, T. M. Lillesand, and P. W. Kiefer, "The use of intensity-hue-saturation transformation for merging SPOT panchromatic and multispectral image data," *Photogramm. Eng. Remote Sens.*, vol. 56, no. 4, pp. 459–467, 1990.

[6] P. S. Chavez, Jr., and A. Y. Kwarteng, "Extracting spectral contrast in landsat thematic mapper image data using selective principal component analysis," *Photogramm. Eng. Remote Sens.*, vol. 55, no. 3, pp. 339–348, 1989.

[7] C. A. Laben and B. V. Brower, "Process for enhancing the spatial resolution of multispectral imagery using pan-sharpening," U.S. Patent 6 011 875, Jan. 4, 2000.

[8] A. Garzelli, F. Nencini, and L. Capobianco, "Optimal MMSE pan sharpening of very high resolution multispectral images," *IEEE Trans. Geosci. Remote Sens.*, vol. 46, no. 1, pp. 228–236, Jan. 2008.

[9] B. Aiazzi, S. Baronti, and M. Selva, "Improving component substitution pansharpening through multivariate regression of MS+pan data," *IEEE Trans. Geosci. Remote Sens.*, vol. 45, no. 10, pp. 3230–3239, Oct. 2007.

[10] X. Otazu, M. Gonzalez-Audicana, O. Fors, and J. Nunez, "Introduction of sensor spectral response into image fusion methods. Application to wavelet-based methods," *IEEE Trans. Geosci. Remote Sens.*, vol. 43, no. 10, pp. 2376–2385, Oct. 2005.

[11] G. Vivone, R. Restaino, M. D. Mura, G. Licciardi, and J. Chanussot, "Contrast and error-based fusion schemes for multispectral image pansharpening," *IEEE Geosci. Remote Sens. Lett.*, vol. 11, no. 5, pp. 930–934, May 2014.

[12] P. S. Chavez, Jr., S. C. Sides, and J. A. Anderson, "Comparison of three different methods to merge multiresolution and multispectral data: Landsat TM and SPOT panchromatic," *Photogramm. Eng. Remote Sens.*, vol. 57, no. 3, pp. 295–303, 1991.

[13] L. Wald and T. Ranchin, "Liu 'Smoothing filter-based intensity modulation: A spectral preserve image fusion technique for improving spatial details'," *Int. J. Remote Sens.*, vol. 23, no. 3, pp. 593–597, Jan. 2002.

[14] B. Aiazzi, L. Alparone, S. Baronti, A. Garzelli, and M. Selva, "MTF-tailored multiscale fusion of high-resolution MS and pan imagery," *photogramm. Eng. Remote Sens.*, vol. 72, no. 5, pp. 591–596, May 2006.

[15] F. Palsson, J. R. Sveinsson, and M. O. Ulfarsson, "A new pansharpening algorithm based on total variation," *IEEE Geosci. Remote Sens. Lett.*, vol. 11, no. 1, pp. 318–322, Jan. 2014.

[16] S. Li and B. Yang, "A new pan-sharpening method using a compressed sensing technique," *IEEE Trans. Geosci. Remote Sens.*, vol. 49, no. 2, pp. 738–746, Feb. 2011.

[17] X. X. Zhu and R. Bamler, "A sparse image fusion algorithm with application to pan-sharpening," *IEEE Trans. Geosci. Remote Sens.*, vol. 51, no. 5, pp. 2827–2836, May 2013.

[18] J. Duran and A. Buades, "Restoration of pansharpened images by conditional filtering in the PCA domain," *IEEE Geosci. Remote Sens. Lett.*, vol. 16, no. 3, pp. 442–446, Mar. 2019.

[19] S. Baronti, B. Aiazzi, M. Selva, A. Garzelli, and L. Alparone, "A theoretical analysis of the effects of aliasing and misregistration on pansharpened imagery," *IEEE J. Sel. Topics Signal Process.*, vol. 5, no. 3, pp. 446–453, Jun. 2011.

[20] J. Duran, A. Buades, B. Coll, C. Sbert, and G. Blanchet, "A survey of pansharpening methods with a new band-decoupled variational model," *ISPRS J. Photogram. Remote Sens.*, vol. 125, pp. 78–105, Mar. 2017.

[21] P. Massip, P. Blanc, and L. Wald, "A method to better account for modulation transfer functions in ARSIS-based pansharpening methods," *IEEE Trans. Geosci. Remote Sens.*, vol. 50, no. 3, pp. 800–808, Mar. 2012.

[22] G. Vivone, M. Simoes, M. Dalla Mura, R. Restaino, J. M. Bioucas-Dias, G. A. Licciardi, and J. Chanussot, "Pansharpening based on semiblind deconvolution," *IEEE Trans. Geosci. Remote Sens.*, vol. 53, no. 4, pp. 1997–2010, Apr. 2015.

[23] F. Palsson, J. R. Sveinsson, M. O. Ulfarsson, and J. A. Benediktsson, "MTF-Based deblurring using a wiener filter for CS and MRA pansharpening methods," *IEEE J. Sel. Topics Appl. Earth Observ. Remote Sens.*, vol. 9, no. 6, pp. 2255–2269, Jun. 2016.

[24] J. Lee and C. Lee, "Fast and efficient panchromatic sharpening," *IEEE Trans. Geosci. Remote Sens.*, vol. 48, no. 1, pp. 155–163, Jan. 2010.

[25] L. Alparone, A. Garzelli, and G. Vivone, "Intersensor statistical matching for pansharpening: Theoretical issues and practical solutions," *IEEE Trans. Geosci. Remote Sens.*, vol. 55, no. 8, pp. 4682–4695, Aug. 2017.

[26] G. Vivone, R. Restaino, and J. Chanussot, "A regression-based high-pass modulation pansharpening approach," *IEEE Trans. Geosci. Remote Sens.*, vol. 56, no. 2, pp. 984–996, Feb. 2018.

[27] Y. Zeng, W. Huang, M. Liu, H. Zhang, and B. Zou, "Fusion of satellite images in urban area: Assessing the quality of resulting images," in *Proc. 18th Int. Conf. Geoinformat.*, vol. 63, Jun. 2010, pp. 691–699.

[28] J. Liu, J. Ma, R. Fei, H. Li, and J. Zhang, "Enhanced back-projection as postprocessing for pansharpening," *Remote Sens.*, vol. 11, no. 6, p. 712, Mar. 2019.

[29] G. Vivone, R. Restaino, and J. Chanussot, "Full scale regression-based injection coefficients for panchromatic sharpening," *IEEE Trans. Image Process.*, vol. 27, no. 7, pp. 3418–3431, Jul. 2018.

[30] A. K. Jain, *Fundamentals of Digital Image Processing*. Hoboken, NJ, USA: Wiley-Blackwell, 1989, pp. 141–168.

[31] M. Li, "Comparison of regularization parameter selection methods in total variation image restoration," M.S. thesis, School Math. Statist., Huazhong Univ. Sci. Technol., Wuhan, China, 2012.

[32] B. Xie, H. K. Zhang, and B. Huang, "Revealing implicit assumptions of the component substitution pansharpening methods," *Remote Sens.*, vol. 9, no. 58, p. 443, 2017.

[33] J. Choi, K. Yu, and Y. Kim, "A new adaptive component-substitution-based satellite image fusion by using partial replacement," *IEEE Trans. Geosci. Remote Sens.*, vol. 49, no. 1, pp. 295–309, Jan. 2011.

[34] S. G. Mallat, "Multiresolution approximations and wavelet orthonormal bases of $L^2(R)$," *Trans. Amer. Math. Soc.*, vol. 315, no. 1, pp. 69–87, Jan. 1989.

[35] M. Irani and S. Peleg, "Improving resolution by image registration," *CVGIP, Graph. Models Image Process.*, vol. 53, no. 3, pp. 231–239, May 1991.

[36] Y. Zhao, R.-G. Wang, W. Jia, W.-M. Wang, and W. Gao, "Iterative projection reconstruction for fast and efficient image upsampling," *Neurocomputing*, vol. 226, pp. 200–211, Feb. 2017.

[37] M. Haris, M. R. Widyanto, and H. Nobuhara, "First-order derivative-based super-resolution," *Signal Image Video Process.*, vol. 11, no. 1, pp. 1–8, Jan. 2017.

[38] M. R. Vicinanza, R. Restaino, G. Vivone, M. D. Mura, G. Licciardi, and J. Chanussot, "A method for improving the consistency property of pansharpening algorithms," in *Proc. IEEE Geosci. Remote Sens. Symp.*, Quebec City, QC, Canada, Jul. 2014, pp. 2534–2537.

[39] M. Irani and S. Peleg, "Motion analysis for image enhancement: Resolution, occlusion, and transparency," *J. Vis. Commun. Image Represent.*, vol. 4, no. 4, pp. 324–335, Dec. 1993.

[40] S. Dai, M. Han, Y. Wu, and Y. Gong, "Bilateral back-projection for single image super resolution," in *Proc. ICME*, Beijing, China, Jul. 2007, pp. 1039–1042.

[41] B. Aiazzi, L. Alparone, S. Baronti, A. Garzelli, and M. Selva, "An MTF-based spectral distortion minimizing model for pan-sharpening of very high resolution multispectral images of urban areas," in *Proc. 22nd Digit. Avionics Syst. Conf.*, Berlin, Germany, May 2004, pp. 90–94.

[42] L. Alparone, L. Wald, J. Chanussot, C. Thomas, P. Gamba, and L. Bruce, "Comparison of pansharpening algorithms: Outcome of the 2006 GRS-S data-fusion contest," *IEEE Trans. Geosci. Remote Sens.*, vol. 45, no. 10, pp. 3012–3021, Oct. 2007.

[43] R. Restaino, G. Vivone, M. D. Mura, and J. Chanussot, "Fusion of multispectral and panchromatic images based on morphological operators," *IEEE Trans. Image Process.*, vol. 25, no. 6, pp. 2882–2895, Jun. 2016.

[44] L. Wald, T. Ranchin, and M. Mangolini, "Fusion of satellite images of different spatial resolutions: Assessing the quality of resulting images," *Photogramm. Eng. Remote Sens.*, vol. 63, no. 6, pp. 691–699, 1997.

[45] R. H. Yuhas, A. F. H. Goetz, and J. W. Boardman, "Discrimination among semi-arid landscape endmembers using the spectral angle mapper (SAM) algorithm," in *Proc. JPL-AVIRIS*, Boulder, CO, USA, 1992, pp. 147–149.

[46] L. Alparone, S. Baronti, A. Garzelli, and F. Nencini, "A global quality measurement of pan-sharpened multispectral imagery," *IEEE Geosci. Remote Sens. Lett.*, vol. 1, no. 4, pp. 313–317, Oct. 2004.

[47] L. Alparone, B. Aiazzi, S. Baronti, A. Garzelli, F. Nencini, and M. Selva, "Multispectral and panchromatic data fusion assessment without reference," *photogramm. Eng. Remote Sens.*, vol. 74, no. 2, pp. 193–200, Feb. 2008.
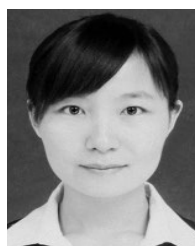
JIAO JIAO received the B.S. degree in computer science and technology from Shanxi University, in 2010, and the M.S. degree in computer application technology from Nankai University, China, in 2013. She is currently pursuing the Ph.D. degree in communication and information systems with Space Engineering University, China.

Her research interests include military information processing and remote sensing image fusion.

LINGDA WU received the B.S., M.S., and Ph.D. degrees in management science and engineering from the National University of Defense Technology, Changsha, China. She is currently a Professor with Space Engineering University, Beijing. Her research interests include military information processing, construction of the battlefield environment, multimedia information systems, and virtual technology.

● ● ●